SUPPLEMENTARY MATERIAL

Polarizing and depolarizing charge injection through a thin dielectric layer in a ferroelectric-dielectric bilayer

Hyeon Woo Park, Seung Dam Hyun, In Soo Lee, Suk Hyun Lee, Yong Bin Lee, Minsik Oh, Beom Yong Kim, Seung Gyu Ryoo, and Cheol Seong Hwang

1. Derivation of a differential form of the inhomogeneous field mechanism (IFM) model

In the present study, the NLS type of switching model was adopted to simulate the ferroelectric switching behavior of the polycrystalline ferroelectric thin films.[1,2] In the framework of the NLS model, the total polarization P_f with respect to time, t, in the polycrystalline ferroelectrics was obtained by integrating the product of local polarization $p(t,\tau)$ and the distribution function $g(\tau)$ of its nucleation time τ as follows:[1,2]

$$\Delta P_f(t) = \int_0^{\infty} g(\tau)p(t,\tau)d\tau \tag{S1.1}$$

As one of the NLS type models, this study adopted the inhomogeneous field mechanism (IFM) model suggested by Zhukov et al. This model assumes that the distribution of the nucleation time in each grain is determined by the distribution of the inhomogeneous field in the disordered polycrystalline thin film.[2] Furthermore, they proposed three main assumptions for this model. First, the local switching of the polarization follows the KAI behavior in each grain with the characteristic time τ as follows:[3]

$$p(t,\tau) = 2P_s\left\{1 - \exp\left[-\left(\frac{t}{\tau}\right)^{\beta}\right]\right\} \tag{S1.2}$$

, where the exponent β represents the dimensionality of the domain propagation, and P_s is the saturated polarization. Second, the basic idea of the IFM model is implemented by the strong dependence of the characteristic time τ on the local field E in the form of Merz's law as follows:

$$\tau(E) = \tau_0\exp\left[\left(\frac{E_a}{E}\right)^{\alpha}\right] \tag{S1.3}$$

, where τ_0 is an intrinsic time constant, E_a denotes an activation field, and α indicates a critical exponent governing the domain dynamics.[4] This field dependence of the switching time has been reported in many ferroelectrics.[5,6] Third, the distribution of inhomogeneous local fields is assumed to be random about the mean value of the applied field $E_m = V/t_f$ when the external voltage V is applied on the film, satisfying a distribution function $Z(E,E_m)$ of the general form:

$$Z(E,E_m) = \frac{1}{E_m}L\left(\frac{E}{E_m}\right) \tag{S1.4}$$

, which is normalized as $\int_0^\infty dEZ(E,E_m) = 1$. In the case of independent switching in each grain, the distribution function is assumed to be Gaussian $L(\xi)$ as follows:

$$L(\xi) = \frac{1}{\sigma\sqrt{2\pi}}\exp\left(-\frac{(\xi-1)^2}{2\sigma^2}\right) \tag{S1.5}$$

, where σ is normalized standard deviation with respect to a normalized variable $\xi = \frac{E}{E_m}$. Since the two switching related variables, the characteristic time τ and the local field E are correlated by Eq. (S1.3), and their distribution functions satisfy the relation $g(\tau)d\tau = Z(E,E_m)dE$, the total summation of the local polarization with respect to time variable, Eq. (S1.1) is transformed into the total summation of the local polarization with respect to the local field variable as follows:

$$\Delta P_f(E_m,t) = \int_0^\infty Z(E,E_m)p[t,\tau(E)]dE \tag{S1.6}$$

The formula is further simplified by noting that the switching behavior of the local polarization $p(t,\tau(E))$ described by Eq. (S1.2) can be approximated by the Heaviside step-function, $2P_s\theta[E - E_{th}(t)]$, where $E_{th}(t)$ is a solution of E in Eq. (S1.3) when the observation time t represents the characteristic time $\tau(E)$ of local polarization. Thus, the total polarization function $\Delta P_f(E_m,t)$ results in a simple form of complementary error function $erfc(x)$ as follows:

$$\Delta P_f(E_m,t) = P_s erfc\left[\frac{\frac{E_{th}(t)}{E_m} - 1}{\sigma\sqrt{2}}\right] \tag{S1.7}$$

Since the solution of the equation $t = \tau(E_{th})$ with $\alpha = 1$ in Eq. (S1.3) is obtained as $E_{th}(t) = E_a/ln(\frac{t}{\tau_0})$, the closed-form of the total polarization with respect to the parameters and the observation time t can be obtained as follows:

$$\Delta P_f(E_m,t) = P_s \mathrm{erfc}\left[\frac{\frac{E_a}{E_m \ln(t/\tau_0)} - 1}{\sigma\sqrt{2}}\right] \tag{S1.8}$$

This final formula of the IFM model has been successfully applied to describe the ferroelectric switching in different types of polycrystalline ferroelectrics such as polycrystalline PZT,[2] and polycrystalline HZO thin films.[7] Nevertheless, unlike the conventional measurement of the switching with a square pulse at a constant voltage, the closed-form of the IFM model cannot be directly applied to simulate the switching behavior under an arbitrary pulse input.[8] Therefore, a generalized form of the IFM model is needed for the following analysis under a ramping bias condition.

In order to simulate a transient response of the polarization with respect to the time-dependent bias, the underlying differential equation has to be used instead of Eq. (S1.8). In this respect, Genenko et al. derived the differential form of the KAI model with the constant characteristic time τ by differentiating the KAI formula, Eq. (S1.2), with respect to time t as follows,[9]

$$\frac{dp}{dt} = \frac{P_s sign(E) - p}{\tau}\beta\left(\frac{t}{\tau}\right)^{\beta - 1} \tag{S1.9}$$

, where $sign(E)$ denotes the polarity of the ferroelectric field E, along which polarization is aligned. This differential equation was generalized, where the ferroelectric field E is no longer constant in time. Moreover, the equation can be applied where τ is also a function of the time-dependent field, as expressed by Eq. (S1.3). The analytical solution of the equation where τ is constant represents the closed form of the KAI model, Eq. (S1.2). Therefore, the underlying differential form of the IFM model is readily derived by differentiating Eq. (S1.6) with respect to time t under the assumption that the intrinsic distribution of the inhomogeneous field is independent of time as follows:

$$\frac{\partial P_f(E_m,t)}{\partial t} = \int_0^\infty Z(E,E_m)\frac{\partial p(t,\tau(E))}{\partial t}dE \tag{S1.10}$$

, where the local switching of p with τ (or the local field E) is governed by the differential equation of the KAI model, Eq. (S1.9). Therefore, by integrating the local switching current density multiplied by the distribution function of the field, the switching current density of the total polarization can be calculated under arbitrary bias. In this study, the Gamma distribution was adopted for the probability density function as follows:

$$Z(E,E_m)dE = f\left(\frac{E}{E_m};k,\theta\right)\frac{dE}{E_m} \tag{S1.11}$$

, where the normalized Gamma distribution is expressed as,

$$f(x;k,\theta) = \frac{1}{\Gamma(k)\theta^k}x^{k-1}e^{-\frac{x}{\theta}} \tag{S1.12}$$

Here, k is a shape parameter, θ represents a scale parameter and $\Gamma(k)$ denotes the gamma function. The Gamma distribution was utilized since it can be transformed to both Poisson-like (exponential) $(k \ll 1)$ and Gaussian-like $(k \gg 1)$ distributions by adjusting the shape parameter.

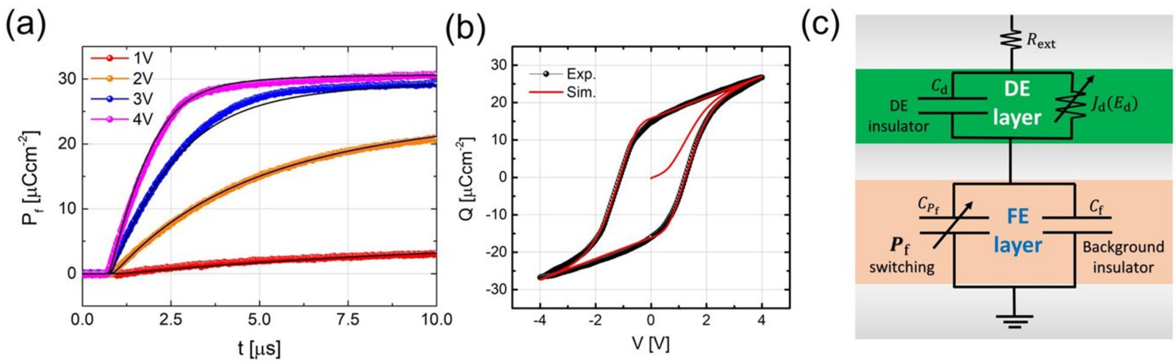

FIG. S1. (a) The ferroelectric polarization was switched by the square pulse, and fitted (black) lines using the differential IFM model. (b) D-V hysteresis using the triangular ramp, and fitted (red) line using the differential IFM model. (c) The equivalent circuit of the ferroelectric-dielectric bilayer structure with the floating metal at the interface.

Figure S1 shows the simulated switching behavior of the HZO thin film under a square pulse and ramp sweep using the differential form of the IFM model. As shown in Fig. S1, not only the time-dependent polarization under the square pulse using pulse measurement device (Fig. S1(a)), but also the hysteresis loop of the total polarization – voltage by the ramping voltage sweep (Fig. S1(b)) using the TF analyzer 2000 was precisely fitted by the differential form of the IFM model derived.

In fact, the equivalent circuit model describes the physics of the bilayer in the 1-dimensional (1-D) framework, which is more appropriate for the MFMDM structure with a constant internal voltage at the interface, as shown in Fig. S1(c). Therefore, the direct comparison between the model and the experimental results was made only during the MFMDM measurement. Nevertheless, based on the similarity between the switching behaviors of MFDM and MFMDM in the experiments, the mechanism of the 1-D model can be reasonably extended to that of the MFDM bilayer structure. This is because even though the 1-D model of the MFMDM structure neglects the inhomogeneity of the potential at the FE/DE interface of the MFDM device, the local spots in the grains, where the injection involved switching occurs, would be approximated to the 1-D model.

2. The effect of sequence between the injection and the switch on the coercive voltage of the bilayer structure.

Tagantsev et al. presented a consistent description of the size effect, demonstrating that the coercive voltage of the stacked-layer (i.e., the MFM structure with the adjacent passive layers) was dependent on both the thickness of the ferroelectric layer and the dielectric layer.[10,11] However, in their model, the dielectric thickness was presumed to be negligibly smaller than the ferroelectric thickness ($\frac{t_d}{t_f} \ll 1$) to simplify the analysis. In this respect, their model of the coercive voltage has limitations for direct application to the ferroelectric-dielectric bilayer structure in which the dielectric thickness was not negligibly small. Therefore, their model should be extended to the more generalized bilayer structure.

As previously pointed out by Tagantsev et al.,[11] the coercive voltage remains unaltered unless the injection through the dielectric layer was involved. In this non-injection switching, the maximum field E_d applied to the dielectric layer should be smaller than the threshold field E_{th} as follows:

$$E_d = \frac{1}{t_d}\left(\frac{C_f}{C_f + C_d}V_t^{max} + \frac{P_f^{max} - \sigma_i}{C_f + C_d}\right) < E_{th} \tag{S2.1}$$

Noting that the $\frac{1}{t_d}\left(\frac{C_f}{C_f + C_d}V_t^{max}\right)$ term of Eq. (S2.1) corresponds to the reference field E_d^L defined as Eq. (6) of the main text, the above inequality can be rewritten as follows:

$$\frac{P_f^{max} - \sigma_i}{C_f + C_d} < \left(E_{th} - E_d^L\right)t_d \tag{S2.2}$$

Since the injected charge σ_i is zero for the non-injection case, Eq. (S2.2) can be expressed as:

$$\frac{P_f^{max}}{C_f + C_d} < \left(E_{th} - E_d^L\right)t_d \tag{S2.3}$$

This equation should be satisfied to induce a non-injection case; otherwise, injection occurs. This result indicates that the maximum polarization switching induced by the applied bias should be lower than a characteristic value $(C_f + C_d)\left(E_{th} - E_d^L\right)t_d$ to prevent the injection. At the apparent coercive voltage of the bilayer (i.e. $V_t = V_c$), the ferroelectric voltage equals the intrinsic coercive voltage of the ferroelectrics as follows:

$$V_c = V_{c0} + E_d t_d \tag{S2.4}$$

Substituting Eq. (S2.1) into Eq. (S2.4), the apparent coercive voltage can be obtained with respect to the polarization P_f and the injected charge density σ_i as follows:

$$V_c = \frac{C_d + C_f}{C_d} V_{c0} + \frac{P_f - \sigma_i}{C_d} \tag{S2.5}$$

It should be noted that the apparent coercive voltage would be larger than the intrinsic coercive voltage if the coercive voltage is defined as the voltage when the ferroelectric polarization is zero ($P_f = \sigma_i = 0$ in Eqn. (S2.5)), as shown in Fig. S2(a). In this study, however, the coercive voltage is defined as the ferroelectric voltage at which the total displacement field is zero (i.e. $D_{tot} = 0$), or

$$P_f = -\epsilon_0 \varepsilon_f E_{c0} = -C_f V_{c0} \tag{S2.6}$$

, where ϵ_0 is the vacuum permittivity, ε_f is the dielectric constant of the FE layer, and $E_{c0}(=\frac{V_{c0}}{t_f})$ is the intrinsic coercive field of the FE layer. By substituting Eq. (S2.6) into Eq. (S2.5), and $\sigma_i = 0$ for the non-injection case, the following relation is obtained,

$$V_c = V_{c0} \tag{S2.7}$$

As for this definition of the coercive voltage, it is shown that the apparent coercive voltage of the ferroelectric-highly insulating dielectric bilayer is identical to the intrinsic coercive voltage of the ferroelectric layer. In respect of the field dimension, this refers to the reduction of the apparent coercive field in the presence of the insulating layer as follows,[11]

$$E_c\left(1 + \frac{t_d}{t_f}\right) = E_{c0} \tag{S2.8}$$

Also, the unvaried coercive voltage of the bilayer without the charge injection can be understood using the load line analysis with respect to the ferroelectric layer, as shown in Fig. S2(b). However, A. Jiang et al. reported the case that the apparent coercive voltage actually decreases as the thickness of the dielectric layer increases.[11] This might be attributed to the smaller coercive field of the ferroelectric subloop since the applied voltage becomes insufficient to induce the fully saturated loop of the ferroelectric layer as the dielectric capacitance decreases.

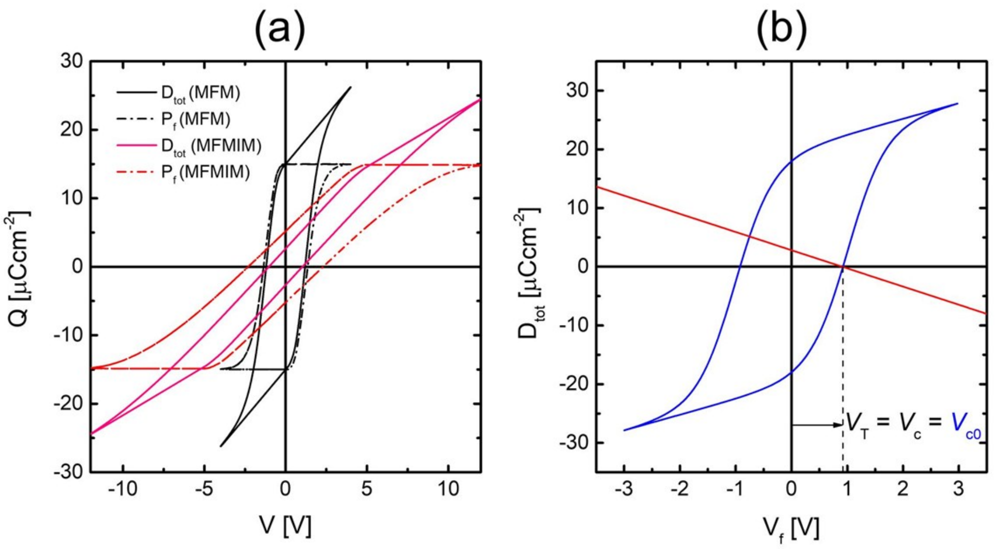

FIG. S2. (a) Simulated hysteresis of D-V and P_f-V curves for the MFM and MFMIM devices. (b) Load line analysis of the MFMIM device. The blue curve represents the D-V hysteresis of the MFM device, and the red line represents the load line of the linear insulating layer when the total voltage V_T equals the intrinsic coercive voltage V_{c0}.

When the injection occurs by the violation of the non-injection condition indicated in Eq. (S4.3), the apparent coercive voltage is affected by the sequence of events, whether the injection or the switching occurs first. If the injection occurs first, the field applied to the dielectric layer E_d should be larger than the threshold field E_{th} at the moment of the ferroelectric switching (i.e. $V_f = V_{c0}$, and $V_t = V_c$) as follows:

$$E_d = \frac{1}{t_d}\left(\frac{C_f}{C_f + C_d}V_c + \frac{P_f - \sigma_{it}}{C_f + C_d}\right) > E_{th} \quad \text{(S2.9)}$$

However, if the injection is not initiated yet at the moment of the ferroelectric switching, the condition should be opposite to Eq. (S2.9) as follows,

$$E_d = \frac{1}{t_d}\left(\frac{C_f}{C_f + C_d}V_c + \frac{P_f - \sigma_i}{C_f + C_d}\right) < E_{th} \quad \text{(S2.10)}$$

These two conditions are confirmed by the simulated results for both cases, as shown in Figs. S3(a) and S3(b). Considering the over/under-compensation of the ferroelectric bound charge, the question remains: Does the over/under-compensation state determine the sequence of injection and switching? At first glance, over-compensation is more likely to induce injection before the switching, as in the case of $\varepsilon_d = 8.9$ in Fig. S3, because the over-compensation state induces higher potential across the dielectric layer than the under-compensation as shown in Fig. S3(c). In order to investigate this assumption, a further modification of the condition is needed.

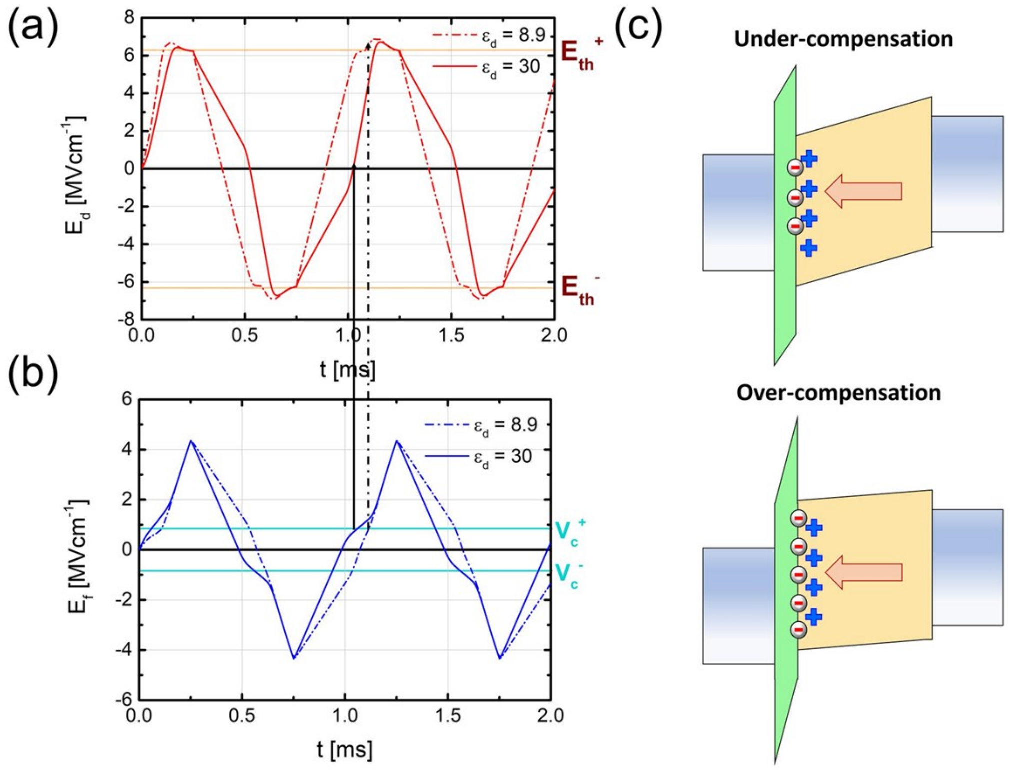

FIG. S3. (a) Fields applied to the dielectric layer plotted in the temporal region. (b) Fields applied to the ferroelectric layer plotted in the temporal region. The dashed curves denote the case for over-compensation ($\varepsilon_d = 8.9$), and the solid curves denote under-compensation ($\varepsilon_d = 30$). (c) Schematics of the band profile for each compensation state when the positive bias is applied to the negatively polarized state.

Supposing that the switching occurs first, and the injection is triggered later, the injection is not turned on yet at the coercive voltage (i.e., $V_f = V_{c0}$, $P_f =- C_f V_{c0}$, and σ_i is still fixed to the previously programmed value). Based on Eq. (S2.5) and Eq. (S2.9), the dielectric field at that moment can be rewritten with respect to the intrinsic coercive voltage V_{c0} as follows:

$$E_d =- \frac{\sigma_{it}}{\epsilon_0 \varepsilon_d} \tag{S2.11}$$

As the electric displacement field is zero at the coercive voltage, the condition that the switching precedes the injection is obtained as follows from Eq. (S2.10) and Eq. (S2.11),

$$E_d = -\frac{\sigma_{it}}{\epsilon_0 \varepsilon_d} < E_{th} \tag{S2.12}$$

Since the injection is not triggered yet, the amount of the injected charge is not altered and remains at the previous value. For example, when the positive bias is applied after the negative poling was performed, σ_{it} in Eq. (S2.12) corresponds to the previous value σ_{it}^{-}, while the threshold field E_{th} in Eq. (S2.12) corresponds to the present positive value E_{th}^{+}. Note that the previous value of the injected charge density $\sigma_{it}^{-} = -\left|\sigma_{it}^{max}\right|$ corresponds to the negatively poled case (i.e., $P_f \rightarrow -\left|P_f^{max}\right|$), and the following displacement field continuity must have been satisfied under the negative poling.

$$-\epsilon_0 \varepsilon_d \left|E_{th}^{-}\right| - \left|\sigma_{it}^{max}\right| = -\epsilon_0 \varepsilon_f \left|E_f^{max}\right| - \left|P_f^{max}\right| \tag{S2.13}$$

, where E_{th}^{-} denotes the threshold field of the dielectric layer during previous negative poling. Also, the following identity is acquired,

$$\epsilon_0 \varepsilon_f \left|E_f^{max}\right| = \left(C_f + C_d\right)\left|E_d^{L}\right| t_d - C_f \left|E_{th}^{-}\right| t_d \tag{S2.14}$$

Once Eq. (S2.13) and Eq. (S2.14) are solved for $\sigma_{it}^{-} = -\left|\sigma_{it}^{max}\right|$, and substituted into Eq. (S2.12), the modified inequality is expressed as follows:

$$\frac{\left|P_f^{max}\right| - \left(C_f + C_d\right)\left(\left|E_{th}^{-}\right| - \left|E_d^{L}\right|\right) t_d}{C_d t_d} < \left|E_{th}^{+}\right| \tag{S2.15}$$

When the Eq. (S2.15) is written with respect to the previous maximum value of the polarization $\left|P_f^{max}\right|$, it can be rewritten as follows,

$$\left|P_f^{max}\right| < C_d \left|E_{th}^{+}\right| t_d + \left(C_f + C_d\right)\left(\left|E_{th}^{-}\right| - \left|E_d^{L}\right|\right) t_d \tag{S2.16}$$

Based on the definition of the capacitance density C_f, the first term on the right side of the inequality is:

$$C_d \left|E_{th}^{+}\right| t_d = \epsilon_0 \varepsilon_d \left|E_{th}^{+}\right| \tag{S2.17}$$

Finally, during the present positive polling, the displacement field is zero ($P_f = -\epsilon_0 \varepsilon_f E_{c0}$) at the coercive voltage, and the following displacement field continuity is satisfied, noting that the injected charge remains at the previous value, $\sigma^-_{it} = -|\sigma^{max}_i|$.

$$\epsilon_0 \epsilon_d |E_d| - |\sigma^{max}_i| = 0 \qquad \text{(S2.18)}$$

Since the switching precedes the injection in this case, the following inequality is satisfied from Eq. (S2.12), and Eq. (S2.18),

$$\epsilon_0 \epsilon_d |E^+_{th}| > |\sigma^{max}_i| \qquad \text{(S2.19)}$$

This inequality is the sequence condition with respect to the injected charge density, while Eqn. (S2.14) is the sequence condition with respect to the switched polarization. In order to satisfy the switching → the injection sequence, both inequalities should be satisfied at the same time. Now the final task is to investigate which compensation condition is compatible with these inequalities. For the over-compensation ($|\sigma^{max}_i| > |P^{max}_f|$) case, it can be shown that both inequalities are satisfied as follows,

$$\epsilon_0 \varepsilon_d |E^+_{th}| + (C_f + C_d)(|E^-_{th}| - |E^L_d|)t_d > |\sigma^{max}_i| + (C_f + C_d)(|E^-_{th}| - |E^L_d|)t_d > |P^{max}_f| \qquad \text{(S2.20)}$$

Since $|E^-_{th}| < |E^L_d|$ in the over-compensation, the middle term of the inequality could be smaller than the last term, $|P^{max}_f|$ as follows,

$$\epsilon_0 \varepsilon_d |E^+_{th}| + (C_f + C_d)(|E^-_{th}| - |E^L_d|)t_d > |P^{max}_f| > |\sigma^{max}_i| + (C_f + C_d)(|E^-_{th}| - |E^L_d|)t_d \qquad \text{(S2.21)}$$

Therefore, this result shows that the over-compensation condition is compatible with the switching → the injection sequence condition. Similarly, for the under-compensation case ($|\sigma^{max}_i| < |P^{max}_f|$), it can be shown that both inequalities are satisfied as follows,

$$\epsilon_0 \varepsilon_d |E^+_{th}| + (C_f + C_d)(|E^-_{th}| - |E^L_d|)t_d > |P^{max}_f| > |\sigma^{max}_i| + (C_f + C_d)(|E^-_{th}| - |E^L_d|)t_d \qquad \text{(S2.22)}$$

Since $|E^-_{th}| > |E^L_d|$ in the under-compensation, the last term of the inequality could be larger than the middle term, $|P^{max}_f|$ as follows,

$$\epsilon_0 \varepsilon_d |E^+_{th}| + (C_f + C_d)(|E^-_{th}| - |E^L_d|)t_d > |\sigma^{max}_i| + (C_f + C_d)(|E^-_{th}| - |E^L_d|)t_d > |P^{max}_f| \qquad \text{(S2.23)}$$

This result shows that the under-compensation condition is also compatible with the switching → the injection sequence condition. Therefore, the switching → the injection condition is independent of the compensation condition since both compensation conditions are compatible with the sequence condition. In the same way, it can be shown that the injection → the switching condition is also compatible with both compensation conditions.

In conclusion, the modified sequence associated with the compensation condition demonstrates that both conditions have no mutual effect, which is consistent with the implication of the compensation condition that the switching related parameters do not affect the compensation state. This is because that the sequence between the injection and the switching is related to the ferroelectric switching related parameters, not to the compensation condition. The sequence is determined by whether or not the dielectric field at the coercive voltage is larger than the threshold field, as expressed by Eq. (S2.12) and Eq. (S2.16). Therefore, the sequence is affected by both the ferroelectric switching parameters, such as the coercive voltage V_{c0}, and the conduction mechanism of the dielectric layer, such as the threshold field E_{th}.

Finally, the effect of the sequence on the apparent coercive voltage was revisited by referring to Eq. (S2.5). Based on Eq. (S2.13) and Eq. (S2.14), the interfacial charge density is solved and substituted into Eq. (S2.5) as follows:

$$V_c = V_{c0} + \frac{\left|P_f^{max}\right| - (C_f + C_d)\left(\left|E_{th}\right| - \left|E_d^L\right|\right)t_d}{C_d} \tag{S2.24}$$

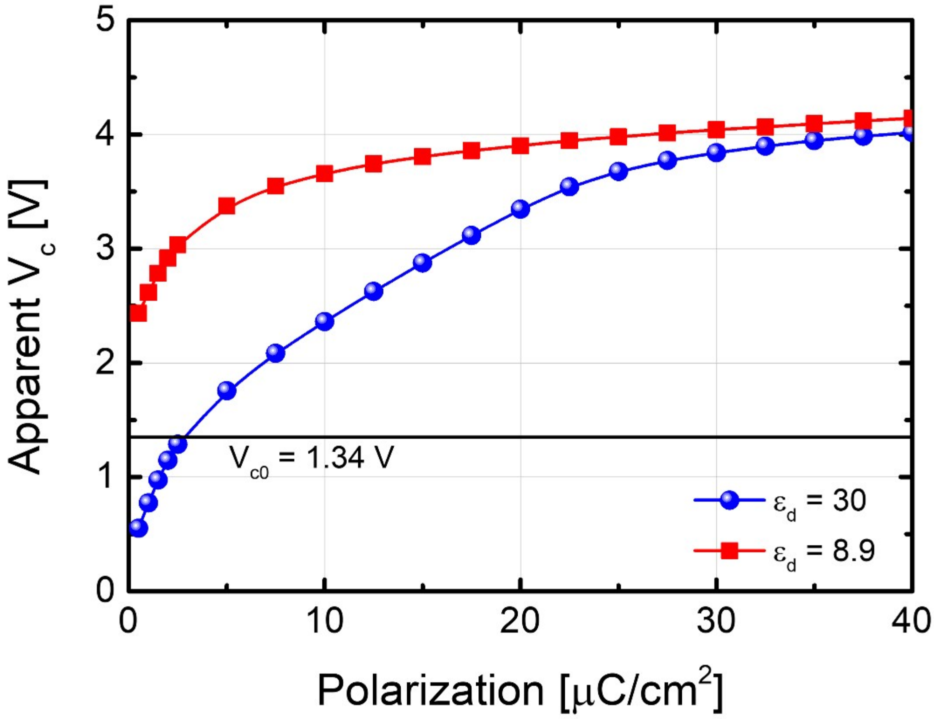

FIG. S4. Apparent coercive voltage V_c plotted with respect to the ferroelectric polarization. Intrinsic coercive voltage V_{c0} of the ferroelectric layer with the saturated polarization, P_s= 20 μCcm^{-2} is denoted by the horizontal black line.

Notably, Eq. (S2.24) is similar to the previous equation derived by Tagantsev et al. in that the apparent coercive voltage is proportional to the maximum switched polarization when the switching precedes the injection.[12] Therefore, the condition for the switching-first is derived based on Eq. (S2.3) and Eq. (S2.16) as follows:

$$(C_f + C_d)\left(|E_{th}| - |E_d^L|\right)t_d < |P_f^{max}| < (C_f + C_d)\left(|E_{th}^-| - |E_d^L|\right)t_d + C_d|E_{th}^+|t_d \quad \text{(S2.25)}$$

If the injection is already turned on at the moment of ferroelectric switching, the following inequality holds:

$$|P_f^{max}| > (C_f + C_d)\left(|E_{th}^-| - |E_d^L|\right)t_d + C_d|E_{th}^+|t_d \quad \text{(S2.26)}$$

, and the apparent coercive voltage is written as a simple linear equation:

$$V_c = V_{c0} + E_{th}t_d \quad \text{(S2.27)}$$

In this case, the dielectric field is nearly fixed to the threshold field E_{th} at the moment. Figure S4 shows the dependence of the apparent coercive voltage on the ferroelectric polarization for the over/under-compensation. Three distinct regions of the switching modes (namely, non-injection, switching before injection, and injection before switching) are identified in the case of under-compensation ($\varepsilon_d = 30$). Note that the apparent coercive voltage can be smaller than that of the single ferroelectric layer (V_{c0} = 1.34 V for the full saturated curve with the saturated polarization, P_s = 20 μCcm^{-2}) due to the decrease of the intrinsic coercive voltage itself as the remanent polarization decreases. However, the apparent coercive voltage is less dependent on the polarization in the case of over-compensation ($\varepsilon_d = 8.9$), as shown in Eq. (S2.27). In the case of over-compensation, the negative value of $|E_{th}| - |E_d^L|$ in Eq. (S2.26) can be large enough, resulting in the inequality regardless of the polarization value. Indeed, it is true that the over-compensation does not necessarily induce the injection before the switching; however, no polarization dependence of the coercive voltage may be observed in the case of over-compensation.

3. Determination of the Laplace field E_d^L and the threshold field E_{th}.

The analytical relationship to estimate the compensation condition was introduced as follows,

$$|E_d^L| < |E_{th}| \text{ (under-compensation)}$$

$$E_d^L = E_{th} \text{ (exact-compensation)} \tag{S3.1}$$

$$|E_d^L| > |E_{th}| \text{ (over-compensation)}$$

This relationship is identified based on the following criteria. Under any circumstances, the continuity of the displacement field is always satisfied at the DE/FE interface as follows:

$$\epsilon_0 \varepsilon_d E_d + \sigma_i = \epsilon_0 \varepsilon_f E_f + P_f \tag{S3.2}$$

When the ferroelectric polarization is switched to $P_{f,max}$ by the maximum field $E_{f,max}$, the dielectric field E_d remains at E_{th} as shown by the nearly constant voltage V_d (fixed at $V_{th} = E_{th} t_d$) in Fig. 3(b) (red line). Thus, from Eq. (S3.2), the maximum injected charge $\sigma_{i,max}$ can be obtained as follows:

$$\sigma_{i,max} = \epsilon_0 \varepsilon_f E_{f,max} + P_{f,max} - \epsilon_0 \varepsilon_d E_{th} \tag{S3.3}$$

After the applied voltage is eliminated, both the residual interfacial charge density, $\sigma_{i,r}$, and polarization, $P_{f,r}$, are retained at their maximal values, as shown in Fig. 2(c). The magnitudes of the two variables are compared based on the following equation:

$$\sigma_{i,r} = P_{f,r} - (\epsilon_0 \varepsilon_d E_{th} - \epsilon_0 \varepsilon_f E_{f,max}) \tag{S3.4}$$

Eq. (S3.4) indicates that the extent of the compensation is directly related to both the magnitude of fields and the dielectric constants in each layer. Under-compensation ($|\sigma_{i,r}| < |P_{f,r}|$) occurs if the magnitude of the former term $\epsilon_0 \varepsilon_d E_{th}$ is larger than that of the latter term in the parenthesis, $\epsilon_0 \varepsilon_f E_{f,max}$, whereas over-compensation ($|\sigma_{i,r}| > |P_{f,r}|$) occurs if the former is smaller than the latter. The physical significance of this condition for the degree of compensation can be further understood from the following discussion. Based on Kirchhoff's voltage law, the relation between the two field variables is expressed as follows:

$$V_{t,max} = E_{th} t_d + E_{f,max} t_f \tag{S3.5}$$

, where $V_{t,max}$ denotes the maximum applied voltage, and $t_d(t_f)$ represents the DE (FE) thickness. Based on Eq. (S3.5), the maximal ferroelectric field is related to E_{th} as follows:

$$E_{f,max} = \frac{V_{t,max}}{t_f} - \frac{t_d}{t_f} E_{th} \tag{S3.6}$$

Then, the inequality which corresponds to the extent of the exact-compensation is revised as follows:

$$\epsilon_0 \varepsilon_f E_{f,max} = \epsilon_0 \varepsilon_d E_{th} \tag{S3.7}$$

Eq. (S3.6) is then substituted into Eq. (S3.7), and then

$$\epsilon_0 \varepsilon_f \left(\frac{V_{t,max}}{t_f} - \frac{t_d}{t_f} E_{th} \right) = \epsilon_0 \varepsilon_d E_{th} \tag{S3.8}$$

Finally, this equation can be further simplified as follows:

$$\frac{1}{t_d} \left(\frac{C_f}{C_f + C_d} V_{t,max} \right) \equiv E_d^L = E_{th} \quad \text{(exact-compensation)} \tag{S3.9}$$

, where $C_f = \frac{\epsilon_0 \varepsilon_f}{t_f}$ denotes the background dielectric capacitance density of the FE layer, and $C_d = \frac{\epsilon_0 \varepsilon_d}{t_f}$ denotes the capacitance density of the DE layer.

On the other hand, the 'turn-on' field E_{th} can also be obtained at the end of the polarization switching (i.e., $\frac{dP_f}{dt} \to 0$ in Eq. (4)) as follows:

$$\epsilon_0 \varepsilon_d \frac{dE_d}{dt} \cong \epsilon_0 \varepsilon_f \frac{dE_f}{dt} - \frac{d\sigma_{it}}{dt} \tag{S3.10}$$

, and the changing rate of the ferroelectric field, E_f, can be obtained from Poisson's equation as follows, under the condition that $\frac{dP_f}{dt} \to 0$,

$$\frac{dE_f}{dt} \cong \frac{1}{t_f}\left(\frac{C_d}{C_d + C_f}\frac{dV_t}{dt} - \frac{1}{C_d + C_f}\left(-\frac{d\sigma_i}{dt}\right)\right) \tag{S3.11}$$

When Eq. (S3.11) is substituted into Eq. (S3.10), the following equation is obtained:

$$\epsilon_0 \varepsilon_d \frac{dE_d}{dt} = \frac{C_d}{C_d + C_f}\left(C_f \frac{dV_t}{dt} - \frac{d\sigma_i}{dt}\right) \to 0 \tag{S3.12}$$

During the 'switch-on' operation, the DE layer acts as the resistor without charging (i.e., $\frac{dE_d}{dt} \to 0$), and thus, the left side of the equation becomes zero. Therefore, the term inside the parenthesis on the right side should also be zero. Therefore, the characteristic 'turn-on' field E_{th} could be obtained from the following equation.

$$C_f \frac{dV_t}{dt} = \frac{d\sigma_i}{dt} = J_d(E_d = E_{th}) \tag{S3.13}$$

4. Verification of the analytical formula for the compensation condition by the numerical simulation.

Depending on the compensation state, either the depolarization field or the polarizing field can be applied to the ferroelectric layer, as shown in Fig. S5(a). The analytical formula, Eq. (S3.1) shows that the charge density – applied voltage ($Q - V_{app}$) relationship for the varying degree of bound charge compensation can be achieved as shown in Fig. S5. For example, the ratio of σ_i to P_f is varied by changing the F-N tunneling barrier, Φ_b, at the TiN/a-AO layer interface, as shown in Figs. S5(b) and S5(c). The tunneling barrier Φ_b was 2.5 and 3.5 eV in Figs. S5(b) and S5(c), respectively, while other parameters of the ramping voltage source were fixed at $V_{t,max} = 6\,V$, and the rising time $t_{rise} = 250\,\mu s$. As Φ_b increases, the carrier injection decreases, and the degree of over-compensation decreases.

The Laplacian field, E_d^L, which provide a reference value in determining the under- or over-compensation, can be readily obtained from Eq. (S3.9) once $V_{t,max}$ is given. On the other hand, the threshold field, E_{th}, can be obtained graphically (see Fig. S5(d)) by plotting the current density–field ($J_d - E_d$) curve, and locating the intersection between the $J_d - E_d$ curve and the horizontal line positioned at J_d, which equals $C_f\frac{dV_t}{dt}$. $C_f\frac{dV_t}{dt}$ value can also be readily obtained from the experimental parameters. Here, the physical implications of E_{th} can be described again as follows. E_{th} is a field value across the DE layer, at which significant current flows (turn on), and is determined by the specific material parameters (C_f, and Φ_b) and experimental voltage ramping conditions ($V_{t,max}$, t_{rise}). When E_{th} is high, the degree of charge injection decreases for the given V_{app}. Given that E_d^L is the field across the DE layer at the specific V_{app} without involving any interfacial charge, it is clear that the condition $|E_d^L| > |E_{th}|$($|E_d^L| < |E_{th}|$) corresponds to over- (under-) compensation.

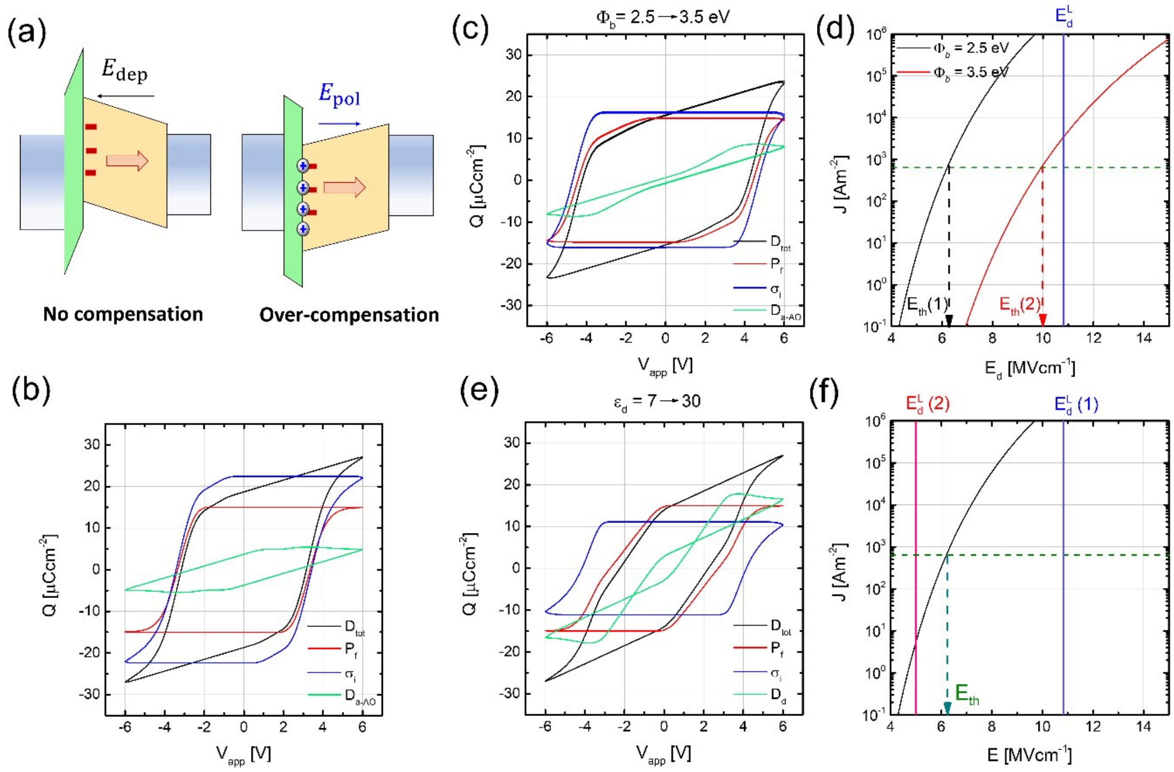

FIG. S5. (a) Schematics of the band diagram profile illustrating the depolarization field and the 'polarizing' field in each compensation state. (b) Separated D-V hysteresis of the MFMDM model with the tunneling barrier $\Phi_b =$ 2.5 eV, and the dielectric constant $\varepsilon_d =$ 7 for reference. (c) Separated hysteresis of the MFMDM model (the lesser over-compensation) by increasing the tunneling barrier to $\Phi_b =$ 3.5 eV. (d) Current density-field characteristics of the dielectric layer. $E_{th}(1)$ corresponds to the MFMDM model of Fig. S5(b), and $E_{th}(2)$ corresponds to the MFMDM model of Fig. S5(c). (e) Separated hysteresis of the MFMDM model (under-compensation) by increasing the dielectric constant to $\varepsilon_d =$ 7. (f) Current density-field characteristics of the dielectric layer. $E_d^L(1)$ corresponds to the MFMDM model of Fig. S5(b), and $E_d^L(2)$ corresponds to the MFMDM model of Fig. S5(e).

Since only the tunneling barrier was modified, the reference field E_d^L was not varied in Fig. S5(d), and was calculated as 10.79 MVcm^{-1} in both cases. Also, the charging current density, $C_f\frac{dV_t}{dt}$, remained the same at 677.40 Am^{-2} in both cases for the given experimental parameters ($V_{t,max} = 6\,V$, and the rising time $t_{rise} = 250\,\mu s$). As seen in Fig. S5(d), E_{th} increased from 6.2 MVcm^{-1} to 9.9 MVcm^{-1}. While E_d^L(= 10.79 MVcm^{-1}) was larger than E_{th} in both cases, the value of E_{th} for the higher tunneling barrier (Φ_b = 3.5 eV) was closer to that of E_d^L. This condition corresponds to the case where the degree of over-compensation was decreased (Fig. S5(c)) compared to the case where Φ_b was lower (2.5 eV, Fig. S5(b)).

Under-compensation can be achieved by increasing the dielectric constant of the DE layer, ε_d, from 7 to 30, as shown in Fig. S5(e). Under this under-compensation condition, the remanent polarization is larger than the injected charge so that the polarity of the effective charge remains the same as that of the polarized bound charge at the interface. The under-compensation condition was also established in Fig. S5(f), representing the $J_d - E_d$ curve. In this case, both the conduction mechanism of the dielectric layer ($\Phi_b = 2.5\ eV$), and the ramping voltage source were not altered, and thus E_{th} remained at 6.2 MVcm^{-1}. However, E_d^L was decreased to 4.93 MVcm^{-1} since the capacitance of the DE layer was increased, as shown in Fig. S5(f). Under-compensation occurs as $E_d^L < E_{th}$, which was verified by the dynamic model, as shown in Fig. S5(e).

As mentioned previously, the injection and switching are not perfectly synchronized, but a time lag exists between the two processes. Tagantsev et al. first recognized the impact of this sequential process and developed a model showing that the apparent V_c of the bilayer was dependent on the specific time difference between the injection and the polarization switching. [10] If the switching precedes the injection, or in other words, the injection is not triggered yet when the ferroelectric field, E_f, reaches the intrinsic coercive field (E_{c0}), the apparent E_c is proportional to P_r.[10] In contrast, if the injection is already turned on before E_f reaches E_{c0}, the apparent E_c becomes independent of P_r, but it becomes proportional to both the thickness t_d and the characteristic field E_{th} of the dielectric layer.[10]

5. Measured I-V and D-V characteristics of the MFM and MDM devices.

Before the proposed experiment using the MFMDM device was performed, each MFM and MDM sample was prepared. As for the MDM device, amorphous Al_2O_3 thin films with top and bottom TiN electrodes were adopted since they showed the ideal reversible characteristic leakage current conduction in addition to the capacitive behavior. Their equivalent circuit is shown in Fig. S6(a). As shown in Fig. S6(a), the MDM device is comprised of two parallel components: the linear capacitor and the nonlinear resistor. When the field applied to the MDM device is small, a negligible leakage current was detected, as shown by the black lines in Fig. S6(b). However, as the field is increased, a significant leakage current induces hysteresis in their D-V curves, as shown by the red lines in Fig. S6(b). Note that these hysteretic curves share the same linear dielectric slope in the middle. Nevertheless, as shown in Fig. S6(c), their nonlinear leakage current is reversible up to the current compliances. Therefore, the parallel nonlinear resistor element of their equivalent circuit can be simplified to a specific nonlinear conduction mechanism, such as F-N tunneling. The dielectric capacitance densities of each thickness (2, 3, 4, and 6 nm) were extracted from the linear slope of the D-V curves. The capacitance densities $C_d$value was estimated as $C_d(2\ nm) = 0.0285\ Fm^{-2}$,$C_d(3\ nm) = 0.0215\ Fm^{-2}$, $C_d(4\ nm) = 0.0152\ Fm^{-2}$, and $C_d(6\ nm) = 0.0101\ Fm^{-2}$. Also, using the capacitance densities, the actual thickness of the samples can be estimated by assuming their dielectric constant as 7 (the dielectric constant of a-Al_2O_3). Their estimated thicknesses were $t_d(2\ nm) = 2.17\ nm$,$t_d(3\ nm) = 2.88\ nm$, $C_d(4\ nm) = 4.08\ nm$, and $C_d(6\ nm) = 6.14\ nm$, which were consistent with the intended thickness values.

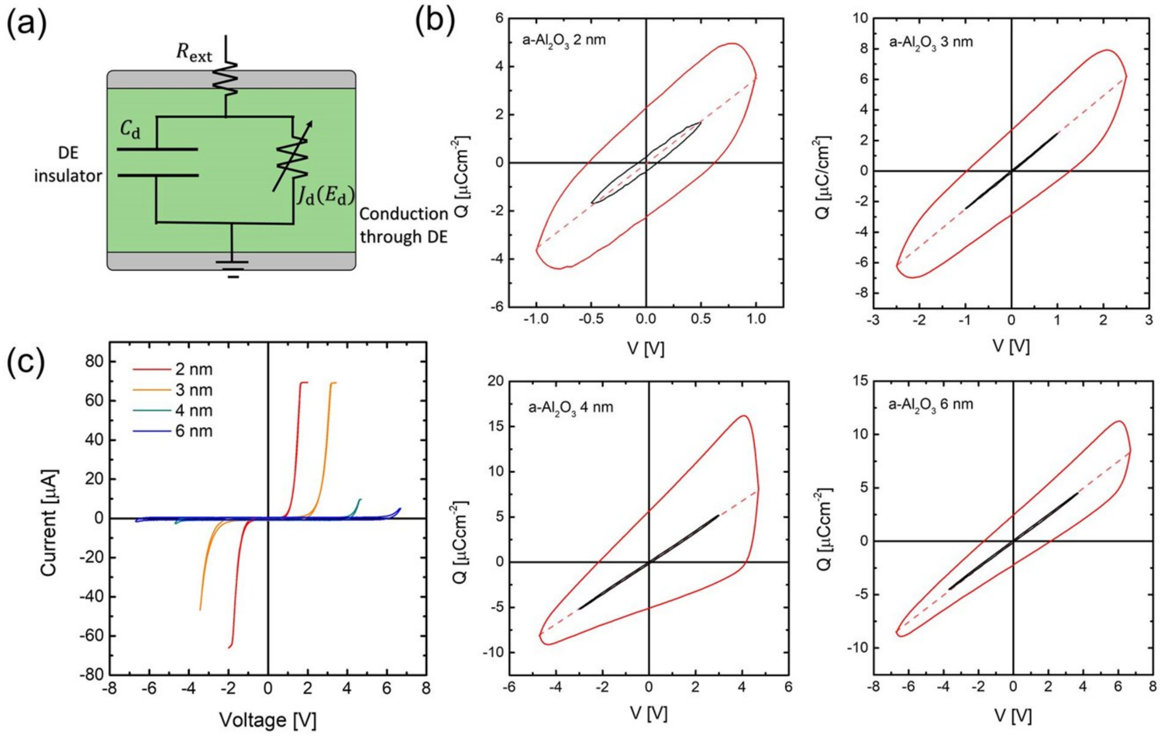

FIG. S6. (a) The equivalent circuit of the MDM device. (b) D-V hysteresis of the amorphous Al_2O_3 devices with various thicknesses (2, 3, 4, and 6 nm). (c) I-V characteristics of the amorphous Al_2O_3 devices with various thicknesses (2, 3, 4, and 6 nm) by the triangular ramp bias.

As for the MFM device, the background dielectric capacitance density of the ferroelectric layer was extracted from the non-switching slope of the D-V curve, as shown in Fig. S7(a). The capacitance density value was estimated as $C_f(10\ nm) = 0.0271\ Fm^{-2}$. Moreover, to establish that the leakage current through the MFM device was negligibly small compared to the conduction through the MDM device, the I-V characteristics of the MFM sample were measured as shown in Fig. S7(b). As shown in the figure, the leakage current through the MFM device was negligible (~0.27 μA at 3 V) compared to that of the MDM device (10~100 μA).

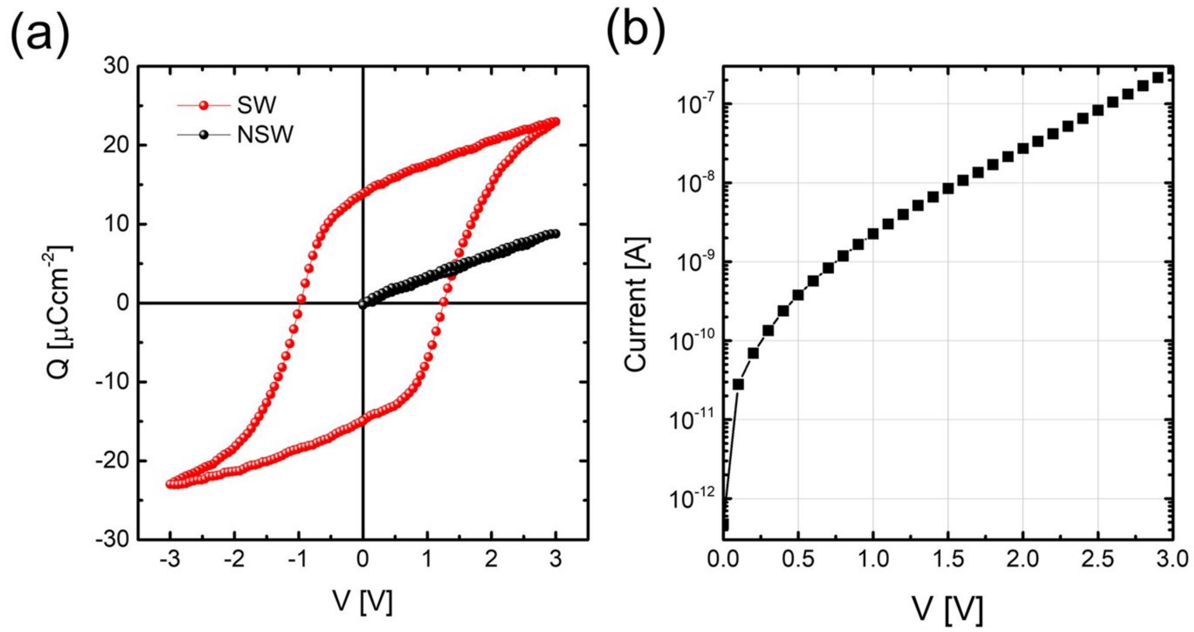

FIG. S7. (a) The non-switching (black) of D-V hysteresis and typical D-V hysteresis of TiN/HZO/TiN film as the MFM device. (b) I-V characteristics of the TiN/HZO/TiN film as the MFM device.

6. Separation of the polarization and the injected charge density by the pulse measurement setup and its validation by the extended circuit simulation

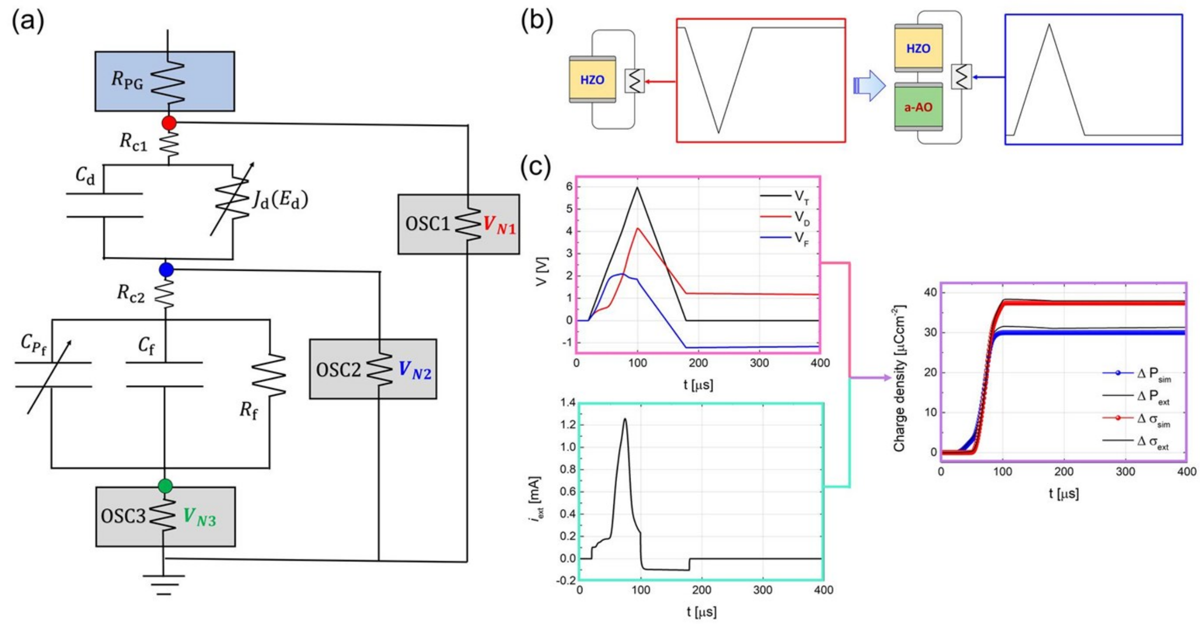

FIG. S8. (a) The extended equivalent circuit of the MFMDM measurement setup. (b) Schematics illustrating the measurement process. (c) Verification of the separation analysis from the extended simulation. The top left figure (magenta) shows the extracted voltages

V_F,V_D,and V_T by referring to the nodal voltages. The bottom left figure (green) shows the measured external current by referring to the nodal voltage on R_{osc3}. The right figure shows that the extracted amount ($\Delta P_{f,mea}$, and $\Delta\sigma_{i,mea}$) of the polarization and the injected charges based on Eq. (S6.4) and Eq. (S6.5) coincides with the actual values ($\Delta P_{f,cal}$, and $\Delta\sigma_{i,cal}$).

Figure S8(a) presents an equivalent circuit of this measurement setup. Initially, the MFM device (i.e., TiN/HZO(9.8 nm)/TiN) was pre-poled in the negative direction by a pulse with an amplitude of -4 V, as shown in Fig. S8(b). The MFM capacitor was then connected serially to the MDM device (i.e., TiN/a-Al_2O_3/TiN) following the setup, and the positive ramping bias was applied to the MFMDM device, as shown in Fig. S8(b). Potentials applied to each layer were obtained from the voltages measured at the three nodes, V_{N1},V_{N2}, and V_{N3}. Based on these node voltages, the voltage on the DE layer, V_D,

$$V_D = V_{N1} - V_{N2} \tag{S6.1}$$

, and the voltage on the FE layer, V_F,

$$V_F = V_{N2} - V_{N3} \tag{S6.2}$$

, and the total voltage over the entire MFMDM device, V_T, is obtained as follows:

$$V_T = V_{N1} - V_{N3} \tag{S6.3}$$

Finally, the externally supplied current i_{ext} entering the MFMDM device was directly obtained from the current measured at node 3 ($i_{ext} = V_{N3}/R_{osc3}$). Based on this setup, the real-time estimation of the injected charges $\Delta\sigma_i(t)$ and the switched polarization $\Delta P_f(t)$ can be achieved as follows:

$$\Delta P_f(t) = \int_0^t i_{ext}(t)dt \; - C_f V_F(t) \tag{S6.4}$$

$$\Delta\sigma_i(t) = \int_0^t i_{ext}(t)dt \; - C_d V_D(t) \tag{S6.5}$$

according to the equivalent circuit of the MFMDM device (Fig. 2(e)) with the known values of the dielectric capacitance density (C_d, and C_f) of each layer. The background capacitance density of the ferroelectric layer was obtained as C_f = 0.0271 Fm^{-2} from the slope of the non-switching charge-voltage curve, as shown in Fig. S7(b).

However, the actual circuit of the measurement (Fig. S8(a)) is slightly different from the desired equivalent circuit (Fig. 2(e)) of the bilayer due to the additional circuit parameters involved, including oscilloscope resistance and parasitic capacitances. Therefore, an additional simulation test based on the actual measurement circuit (Fig. S8(a)) was performed to confirm the validity of this analysis. As shown in Fig. S8(c), the simulation established that the additional elements resulted in negligible errors (< 4.2%) between the values assuming the presence of the oscilloscope ($\Delta\sigma_{i,mea}$(blue dots), and $\Delta P_{f,mea}(red\ dots)$, and in the absence of it (corresponding to the circuit in Fig. 2(e)) ($\Delta\sigma_{i,cal}$, and $\Delta P_{f,cal}$, both with black lines on the right side of Fig. S8(c)) using the aforementioned theoretical model. This result implies that the influence of the added circuit factors related to the oscilloscope can be ignored due to the substantially higher oscilloscope resistances ($R_{osc1} = R_{osc1} =$ 1 MΩ, but $R_{osc3} =$ 50 Ω) compared with the effective impedance of the MFMDM sample. It should be noted that both data sets are simulation results assuming the presence and absence of the oscilloscope. A more detailed method of the extended circuit simulation is introduced in the supplementary material.

The actual circuit for the MFMDM measurement is more complex than the simple equivalent circuit of the bilayer alone, as shown in Fig. S1(c). This is because of the need to include additional impedances to determine the nodal voltages in the actual measurements, as shown in Fig. S8(a). Figure S9 shows the extended equivalent circuit of Fig. S8(a) where the parasitic capacitances of the oscilloscope were included. Since these parasitic capacitances may influence the overall accuracy of the separation technique, their effects should be investigated using the extended circuit, as shown in Fig. S9.

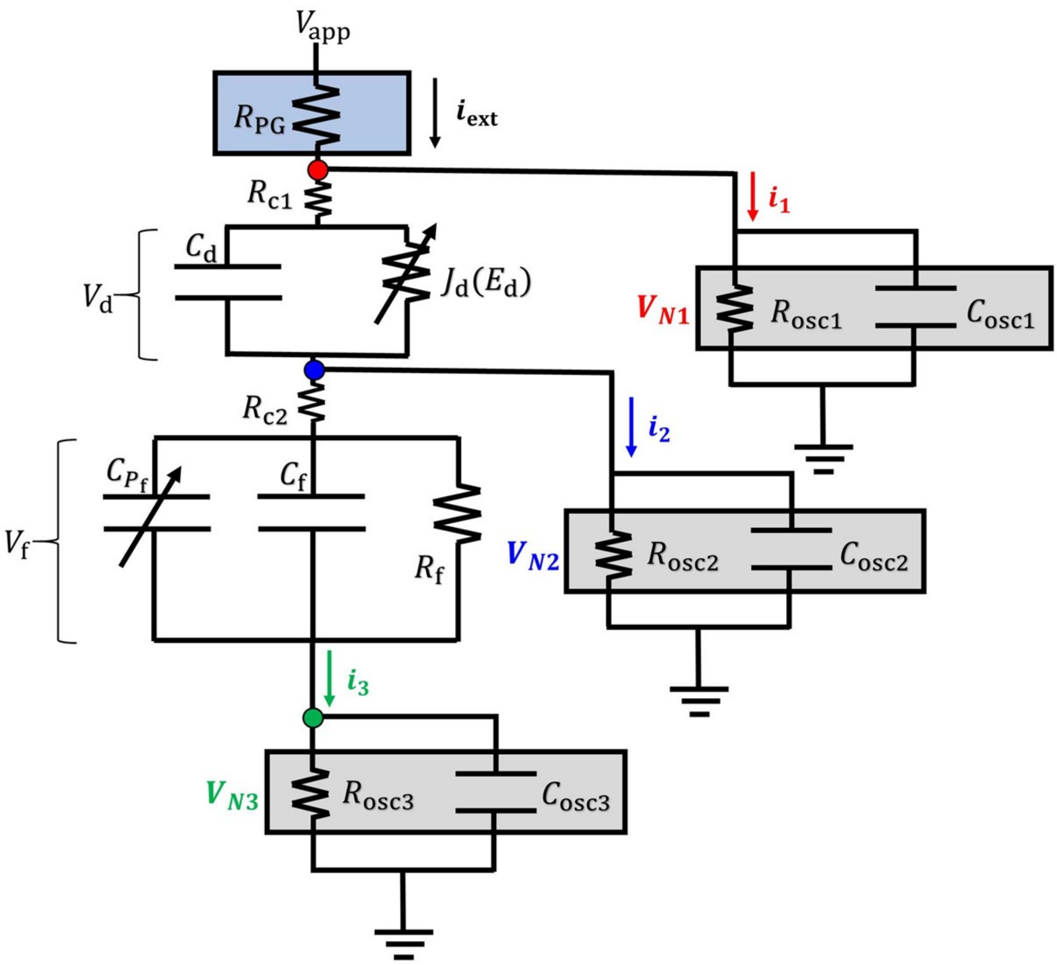

FIG. S9. The extended equivalent circuit of the MFMDM measurement setup including the parasitic capacitors of the oscilloscope.

Due to these parasitic components, before the model analysis was performed based on the measurement results, the circuit simulation in which the same parasitic elements are included should be verified such that the extracted values from the model analysis yield the same values as the targeted switching and injection quantities. The circuit simulation can be performed as follows. Based on Kirchhoff's voltage and current laws, the following four equations should be satisfied simultaneously:

$$V_{N1} = V_f + R_{c1}(i_{ext} - i_1) + V_d + R_{c2}i_3 + V_{N3} \tag{S6.6}$$

$$V_{N2} = V_f + R_{c2}i_3 + V_{N3} \tag{S6.7}$$

$$R_{PG}i_{ext} = V_{app} - V_{N1} \tag{S6.8}$$

$$i_{ext} = i_1 + i_2 + i_3 \tag{S6.9}$$

, where R_{osc}denotes the resistance of the nodal impedance ($R_{osc1} = R_{osc2} = 1\ M\Omega$, and $R_{osc3} = 50\ \Omega$); C_{osc} denotes the parasitic capacitance of the nodal impedance ($C_{osc1} = C_{osc2} = C_{osc3} = 100\ pF$); R_c denotes the contact resistance form the probe to the devices ($R_{c1} = R_{c2} = 50\ \Omega$); R_f represents the leakage current through the ferroelectric layer ($R_f = 10^{10}\Omega$); and R_{PG} is the internal resistance of the pulse generator ($R_{PG} = 50\ \Omega$). The following set of equations can be obtained for each current component:

$$i_{ext} = \frac{V_{app} - V_{N1}}{R_{PG}} \tag{S6.10}$$

$$i_1 = \frac{V_{app} - V_{N1}}{R_{PG}} - \frac{V_{N1} - V_{N2} - V_d}{R_{c1}} \tag{S6.11}$$

$$i_2 = \frac{V_{N1} - V_{N2} - V_d}{R_{c1}} - \frac{V_{N2} - V_f - V_{N3}}{R_{c2}} \tag{S6.12}$$

$$i_3 = \frac{V_{N2} - V_f - V_{N3}}{R_{c2}} \tag{S6.13}$$

Then, the nodal voltages are readily acquired from the continuity equations as follows,

$$\frac{dV_{N1}}{dt} = \frac{1}{C_{osc1}}\left(\frac{V_{app} - V_{N1}}{R_{PG}} - \frac{V_{N1} - V_{N2} - V_d}{R_{c1}} - \frac{V_{N1}}{R_{osc1}}\right) \tag{S6.14}$$

$$\frac{dV_{N2}}{dt} = \frac{1}{C_{osc2}}\left(\frac{V_{N1} - V_{N2} - V_d}{R_{c1}} - \frac{V_{N2} - V_f - V_{N3}}{R_{c2}} - \frac{V_{N2}}{R_{osc2}}\right) \tag{S6.15}$$

$$\frac{dV_{N3}}{dt} = \frac{1}{C_{osc3}}\left(\frac{V_{N2} - V_f - V_{N3}}{R_{c2}} - \frac{V_{N3}}{R_{osc3}}\right) \tag{S6.16}$$

Finally, using the identified currents, the continuity equations can be readily solved in each device coupled with the implemented model equations in each layer**.** As shown in Fig. S8(c) of the main text, the extended circuit simulation verified that the extracted value from the model analysis coincides with (the relative error < 4.2 % at most) the actual values of the switched and injected amounts.

7. Degradation of the resolution for the externally measured current in the pulse experiments.

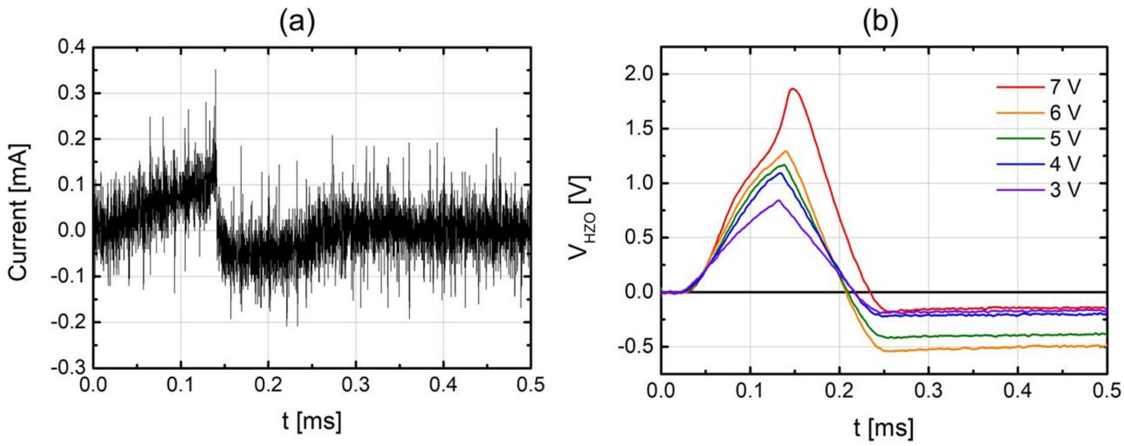

FIG. S10. (a) Degraded resolution of the measured external current of the MFMDM device with 4 nm a-Al_2O_3 when the peak of the applied voltage is 6 V at 2.5 kHz frequency. (b) Measured ferroelectric voltage with the same condition.

Depending on the size of the sample or the applied pulse condition, the resolution of the measured external current using the device can be severely degraded, as shown in Fig. S10(a). In this case, the accurate estimation of the total displacement field is difficult, so that the overall separation analysis is also hindered. Indeed, while the limitation of the analysis depends on the specific measurement device, a certain boundary exists beyond which the accurate measurement of the current is unavailable. Nevertheless, the voltage applied to the sample can be measured within an acceptable range of the oscilloscope, even when the current is too small to be measured, as shown in Fig. S10(b). Therefore, the effective charge density can be estimated based on this voltage without measuring the electric noise.

The effective net charge density, $\Delta\sigma_i - \Delta P_f$, can be obtained using the following procedure. In principle, the residual quantity of the total displacement field, ΔQ_{res}, is first obtained by integrating the circuit current i_{ext} as follows:

$$\Delta Q_{res} = \int_0^{t_{final}} i_{ext} dt \tag{S7.1}$$

Based on the current continuity condition (Fig. 2(e)), i_{ext} is decomposed to the charging current $i_{cc}(DE)$ and the leakage current $i_{leak}(DE)$ in the dielectric layer. Also, in the ferroelectric layer, the i_{ext} is identical to the sum of the charging current $i_{cc}(FE)$ and the switching current $i_{sw}(FE)$ as follows:

$$i_{ext} = i_{cc}(DE) + i_{leak}(DE) = i_{cc}(FE) + i_{sw}(FE) \tag{S7.2}$$

Therefore, the ΔQ_{res} can be expressed as the sum of two charge components in each layer as follows:

$$\Delta Q_{res} = \Delta Q_d + \Delta \sigma_i = \Delta Q_f + \Delta P_f \tag{S7.3}$$

, where $\Delta Q_d$and ΔQ_f denote the charge amounts in each capacitor, respectively. Based on the dielectric capacitance of each layer, Eq. (S7.3) can be rewritten as

$$\Delta Q_{res} = C_d \Delta V_d + \Delta \sigma_i = C_f \Delta V_f + \Delta P_f \tag{S7.4}$$

During the discharging, the sum of the ferroelectric and dielectric voltages equals zero, i.e., $V_d(t_{final}) + V_f(t_{final}) = 0$, thus,

$$\Delta V_d = -\Delta V_f \tag{S7.5}$$

Substituting this relation into Eq. (S7.4), and it was solved for the discharging voltage of the ferroelectric layer, $V_{f,dis}$, as follows:

$$\Delta V_f \equiv V_{f,dis} = -\frac{\Delta P_f - \Delta \sigma_i}{C_d + C_f} \tag{S7.6}$$

Based on this equation, the effective amount of the charge at the interface can be directly obtained from the discharging voltage without referring to the i_{ext} as follows:

$$\Delta \sigma_i - \Delta P_f = (C_d + C_f) V_{f,dis} \tag{S7.7}$$

8. 2-dimensional injection involved switching model of the metal-ferroelectric-dielectric-metal MFDM structure.

The presented 1-D dynamic model revealed the fundamental physics of the injection involved switching mechanism of MFMDM device. However, it should be noted that this simplified equivalent circuit model (Fig. S1(c)) is not comprehensive enough to describe precisely the complicated inhomogeneity inside the ferroelectric layer. This is because this model does not take into consideration the probable variation of the material parameters along with the lateral dimension of the thin films, which could be disregarded in the 1-D model by the presence of the intermediate metal layer. However, in the more practical MFDM cases, there is no intervening M layer, so it is necessary to extend the simple 1-D model to the 2-D case to investigate the physics of the injection involved switching in the MFDM structure. The polycrystalline ferroelectric layer, such as the HZO film, is spatially inhomogeneous, and the injection or switching path may also be inhomogeneous along with the lateral dimension. It was reported that the electric field in disordered polycrystalline materials becomes inhomogeneous mainly for two reasons.[9]

1) The random spatial dielectric tensor along with the local crystalline orientation of individual grains

2) The bound charges at the grain boundaries resulted from the discontinuous polarization at the grain boundaries.

Other structural factors, such as local film thickness variation and the local involvement of the non-ferroelectric phases, can also influence the switching parameters and dynamical behavior. However, in this section, the two major factors mentioned above were considered.

At first, considering that the polycrystalline ferroelectric layer has a column-like grain structure,[13] each column in the ferroelectric layer shown in Fig. S11 represents the single grain with its specific crystallographic orientation. It was assumed that all the grains have an identical size of 10 nm, and each grain is supposed to exhibit a random crystal orientation arbitrarily chosen from the interval $\theta_m - \frac{\pi}{6} \leq \theta \leq \theta_m + \frac{\pi}{6}$ with the central value of $\theta_m = \pm\frac{\pi}{3}$. This is because the typical spontaneous polarization value of the HZO is usually half of the theoretical one (P_r ~ 50 μCcm^{-2}) calculated from the DFT theory.[14]

The local polarization vector within each grain, p_i, is supposed to be uniform, and the polarization reversal is dominated by 180° domain wall motion so that the polarization changes along only one principal direction of each grain. In this case, the polarization reversal in each grain can be effectively modeled by the generalized KAI model as follows,[9]

$$\frac{dp_i}{dt} = \frac{n_i P_s sign(\langle E\rangle_i \cdot n_i) - p_i}{\tau_i}\beta\left(\frac{t}{\tau_i}\right)^{\beta - 1} \tag{S8.1}$$

, where n_i is the unit vector in the principal direction in each grain, τ_i is the characteristic time constant in each grain, and $\langle E\rangle_i$ is the spatial average of the electric field in each grain. The electric field distribution is evaluated by solving the 2-D Poisson's equation with COMSOL multi-physics package, the commercial finite element software. While the equation for the switching kinetics is approximated to be a 1-D process along the principal axis in each grain, the 2-D coupling between the grains is incorporated into the local field-dependent switching time as follows,

$$\tau_i = \tau_0 \exp\left(\frac{E_a}{|\langle E\rangle_i \cdot n_i|}\right) \tag{S8.2}$$

, where τ_0 is the intrinsic time constant, and E_a is the activation field of the switching. As for the conduction through the dielectric layer above each ferroelectric grain, the similar coarse-graining approximation inside each grain was adopted as follows,

$$J_i = J_{tu}(\langle E\rangle_i \cdot n_z) \tag{S8.3}$$

, where J_{tu} represents the corresponding tunneling formula of the dielectric layer, and n_z is the unit vector along with the vertical direction to the FE/DE interface. The injected charge is supposed to be accumulated on the FE/DE interface of each grain. Finally, the periodic boundary condition was applied at the left and right sides of the simulation domain. Based on this 2-D formulation, the effect of the spatial inhomogeneity on the injection involved switching of the MFDM structure was simulated.

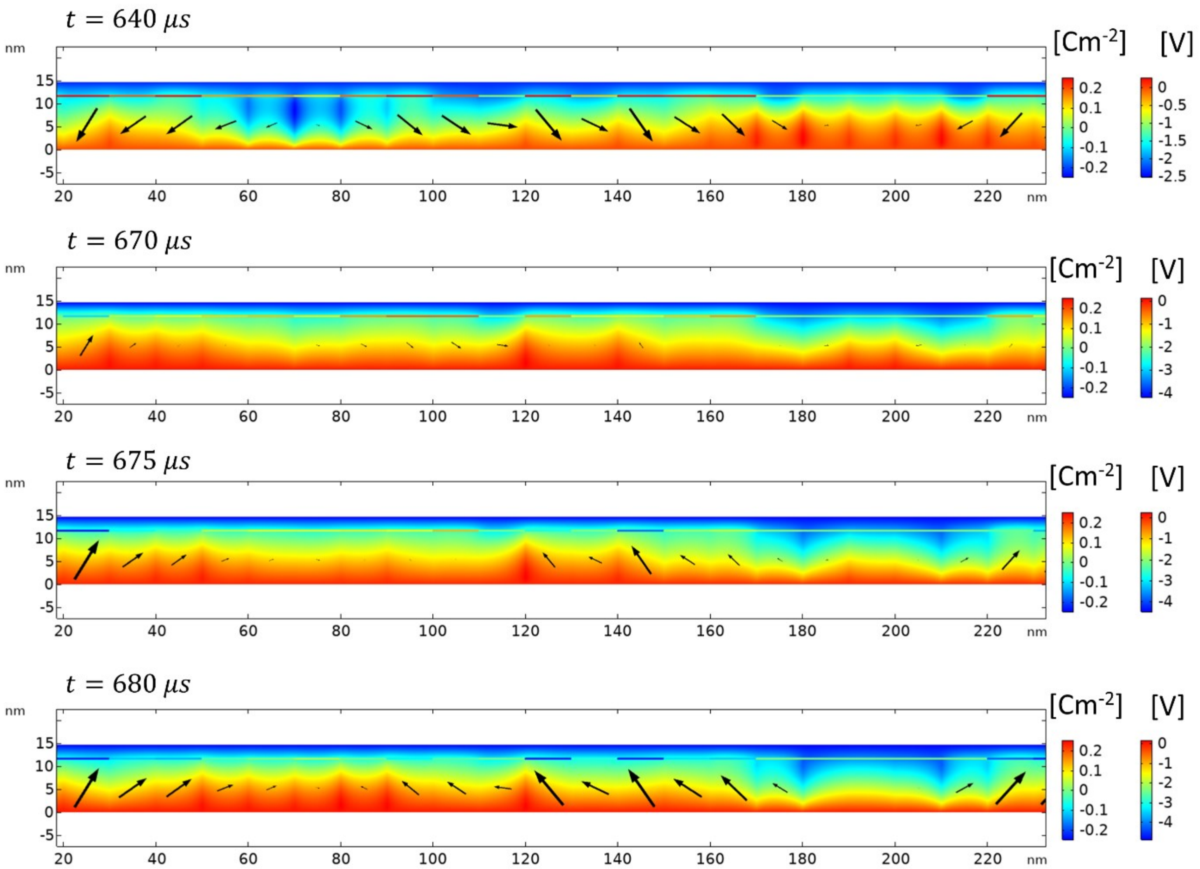

FIG. S11. Injection-involved switching process of the MFDM structure. In each figure, the upper layer is the dielectric layer, and the lower layer is the ferroelectric layer. Arrows in each grain denote the polarization vector, and the surface color represents the electrical potential. The injected charge density at the FE/DE interface is denoted by the color legend on the right side.

Figure S11 shows the injection involved switching process of the MFDM structure. Initially, at 640 μs, the polarization in each grain is poled to the downward direction, and the compensated charge at the interface in each grain has a positive polarity. It is noteworthy that the polarization near the abrupt crystal orientation boundary (i.e., θ_m from $\sim \pm\frac{\pi}{3}$ to $\sim \mp\frac{\pi}{3}$) shows depoled states due to the large depolarization field. As the applied voltage increases, the injection involved switching occurs first in the grain in which the crystal orientation is closest to the vertical direction. This is because the field across the principal polarization direction is the largest in this grain. However, it is noteworthy that the polarization switching in the neighbor grain of the switched one always occurs next, irrespective of their crystal orientations. This is because the additional bound charge at the grain boundary emerges as the first polarization is switched. The compensation of this bound charge is not as sufficient as that of the bound charge at the FE/DE interface, and the emerging bound charge at the grain boundary triggers the immediate polarization switching in the neighbor grains.

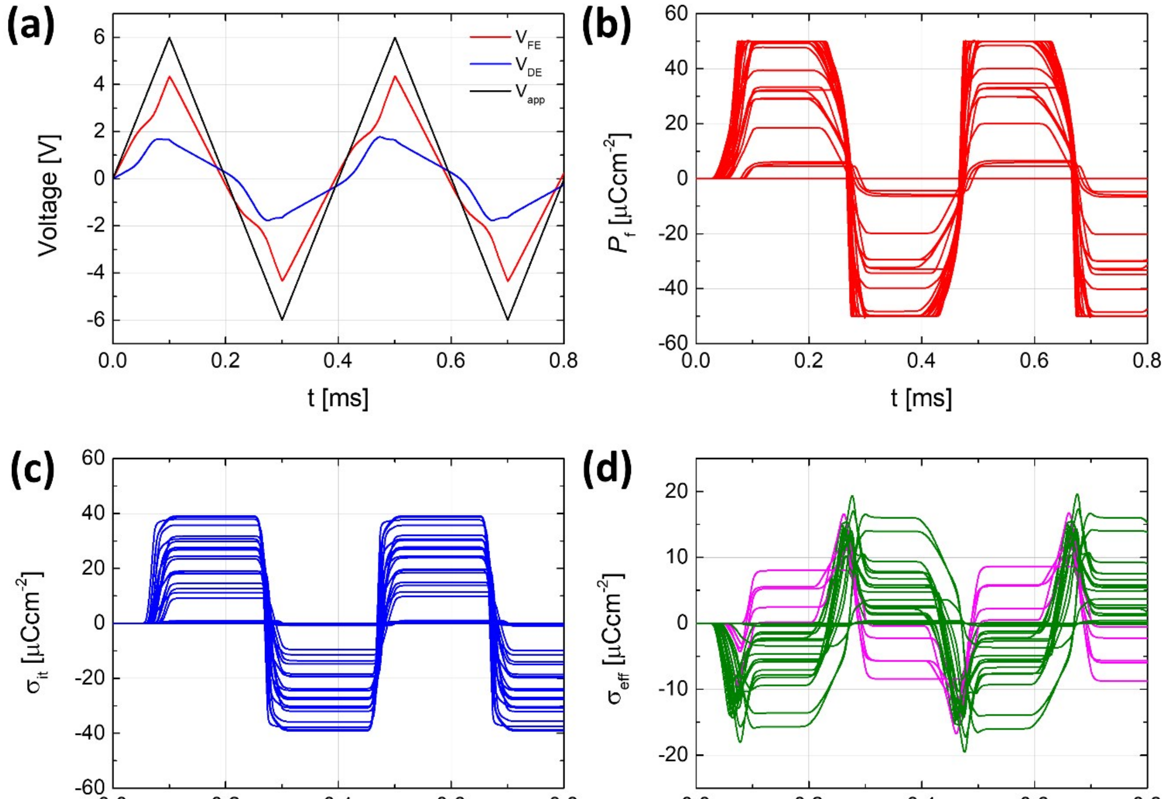

FIG. S12. (a) The time evolution of the internal averaged voltages (red: averaged FE voltage, blue: averaged DE voltage), and the applied ramp voltage (black). (b) The time evolution of the polarizations in each grain. Each red line corresponds to the polarization in each grain. (c) The time evolution of the injected charge density at the interface in each grain. Each blue line corresponds to the interfacial charge density in each interface. (d) The time evolution of the effective total charge density at the interface in each grain. The green curves represent the effective charges with the under-compensation state, and the magenta curves represent the effective charges with the over-compensation state.

Figure S12 shows the time evolution of the polarization and the injected charge density at the FE/DE interface in each grain. As shown in Fig. S12(a), the averaged voltage in each layer shows a similar aspect as that of the charging curve calculated from the 1-D model. It should be noted that the negative feedback on the DE layer during the injection involved switching can still be found in the 2-D model. Also, as shown in Figs. S12 (b) and (c), the injection involved switching in each grain is not a synchronized process, and the polarized value is ranged from ~ 5 μCcm^{-2} to 50 μCcm^{-2}. Nevertheless, the overall injected charge density seems to be smaller (~ 0.4 μCcm^{-2} to 40 μCcm^{-2}) than the switched polarization, which corresponds to the under-compensation case. Figure S12(d) shows the time evolution of the effective total charge at the FE/DE interface. As shown in the figure, the compensation state is not necessarily homogeneous over the entire area. In general, the under-compensation (negative total effective charge at the interface for the downward polarization) is dominant. However, in a few grains (denoted by the magenta lines in Fig. S12(d)), the over-compensation (positive total effective charge density at the interface for the downward polarization) actually occurs. Nevertheless, this MFDM structure remained at the overall under-compensation state, as shown in the averaged displacement field versus the applied voltage (Fig. S13(a)).

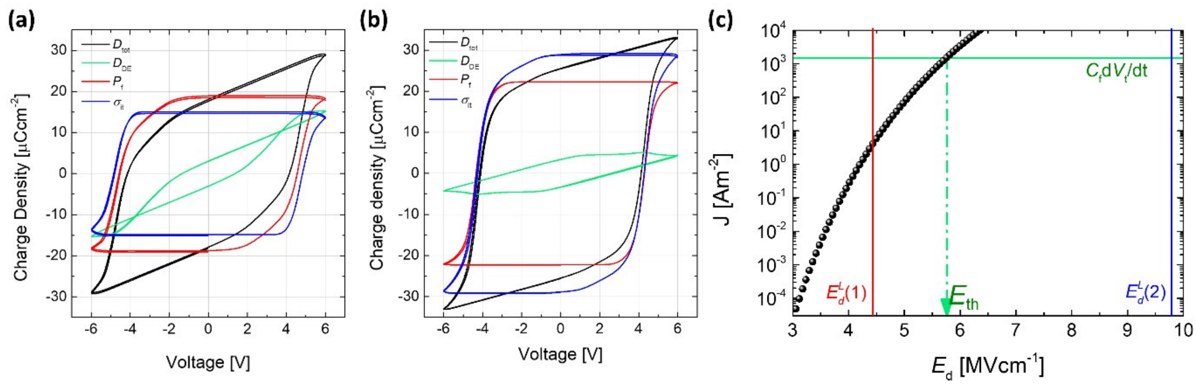

FIG. S13. (a) Averaged displacement field (D) – applied voltage (V) curve with the dielectric constant ε_d of 30. The red curve denotes the averaged polarization, and the blue curve denotes the averaged injected charge density at the interface. The charge accumulated on the dielectric layer is indicated by the green curve. (b) Averaged displacement field (D) – applied voltage (V) curve with the dielectric constant ε_d of 8.9. (c) Current density(J) – field(E) plot of the dielectric layer, and the comparison of the characteristic fields E_d^L and E_{th}. The red line denotes E_d^L for the former case (Fig. S13(a), $\varepsilon_d = 30$), and the blue line denotes E_d^L for the latter case (Fig. S13(b), $\varepsilon_d = 8.9$).

Figure S13(a) and (b) show the change in the averaged displacement field versus the applied voltage of MFDM from the (a) under-compensation state to (b) over-compensation state by varying the dielectric constant ε_d of the dielectric layer from (a) 30 to (b) 8.9. Figure S13(c) shows that the averaged compensation condition can be still estimated by comparing the macroscopic values E_D^L and E_{th} based on the hypothesis that the conduction mechanism of the DE layer is not altered in the presence of the FE layer. This result corroborates that these macroscopic values E_D^L and E_{th} represent the overall compensation condition of MFDM structure even though the local compensation state in the small portion might be different from the averaged state. Moreover, it should be noted that the remanent polarization estimated from the total displacement field versus applied voltage ($D-V$ loop) is always larger (smaller) than the actual value for the over (under)-compensation. As expected, this result is consistent with the analytical model (Eqn. 10) for the homogeneous MFMDM structure as the total charge density at the uniformly poled state can be effectively estimated by the macroscopic variables.

REFERENCES

[1]A. K. Tagantsev, I. Stolichnov, and N. Setter, *Phys. Rev. B.*, 2002, **66**, 214109.

[2]S. Zhukov, Y. A. Genenko, and H. von Seggern, *J. Appl. Phys.*, 2010, **108**, 014106.

[3]Y. Ishibashi, and Y. Takagi, *J. Phys. Soc. Jpn.*, 1971, **31**, 506.

[4]J. Y. Jo, D. J. Kim, Y. S. Kim, S.-B. Choe, T. K. Song, J.-G. Yoon, and T. W. Noh, *Phys. Rev. Lett.*, 2006, **97**, 247602.

[5]W. J. Merz, *J. Appl. Phys.*, 1956, **27**, 938.

[6]H. H. Wieder, *J. Appl. Phys.*, 1960, **31**, 180.

[7]S. D. Hyun, H. W. Park, Y. J. Kim, M. H. Park, Y. H. Lee, H. J. Kim, Y. J. Kwon, T. Moon, K. D. Kim, Y. B. Lee, B. S. Kim, and C. S. Hwang, *ACS. Appl. Mater. Interfaces*, 2018, **10**, 35374-35384.

[8]S. L. Miller, J. R. Schwank, R. D. Nasby, and M. S. Rodgers, *J. Appl. Phys.*, 1991, **70**, 2849.

[9]Y. A. Genenko, J. Wehner, and H. von Seggern, *J. Appl. Phys.*, 2013, **114**, 084101.

[10]A. K. Tagantsev, and I. A. Stolichnov, *Appl. Phys. Lett.*, 1999, **74**, 1326.

[11]A. Q. Jiang, M. Dawber, J. F. Scott, C. Wang, P. Migliorato, M. Gregg, *Jpn. J. Appl. Phys.*, 2003, **42**, 6973.

[12]A. K. Tagantsev, M. Landivar, E. Colla, and N. Setter, *J. Appl. Phys.*, 1995, **78**, 2623.

[13]M. Pešić, F. P. G. Fengler, L. Larcher, A. Padovani, T. Schenk, E. D. Grimley, X. Sang, J. M. LeBeau, S. Slesazeck, U. Schroeder, T. Mikolajick, *Adv. Funct. Mater.*, 2016, **26**, 4601.

[14]S. Clima, D. J. Wouters, C. Adelmann, T. Schenk, U. Schroeder, M. Jurczak, G. Pourtois, *Appl. Phys. Lett.*, 2014, **104**, 092906.